

## ARTICLE OPEN



# Inter-model robustness of the forced change of the ENSO-Indian Summer Monsoon Teleconnection

Sundaresan Aneesh<sup>1,2</sup> and Tamás Bódai<sup>1,2,3</sup>

Concerning the robustness of predicting the forced response of the El Niño—Southern Oscillation-Indian summer monsoon (ENSO-ISM) teleconnection based on 9 CMIP-class models, we come to distinguish three time periods. (1) In the late 20th century, the trend was insignificant in most models, which does not permit a statement on robustness in this period. Thus the weakening of the teleconnection reported from the observational data might not be truly forced. (2) Furthermore, we find it typical that under global warming in the first part of the 21st century, the teleconnection is strengthening or non-decreasing. This considerable inter-model robustness is owed to an increasing ENSO variability as well as coupling strength. (3) At the end of the 21st century, however, under strong forcing, the teleconnection change is not robustly modeled: the ENSO variability change is not projected robustly across models, either with respect to the start or the rate of the ENSO variance decline, competing this time with an increase of the coupling strength. The difference in the projected coupling coefficient between models is mainly attributed to the disagreement in the projected ENSO-induced changes in the regional Hadley cell and SST patterns over the ISM domain, despite the agreement on the projected eastward shift of the Walker cell over the Pacific Ocean.

*npj Climate and Atmospheric Science* (2024)7:4; <https://doi.org/10.1038/s41612-023-00541-w>

## INTRODUCTION

The El Niño—Southern Oscillation (ENSO) is the climate variability that is reigning supreme in the tropics, significantly modulating the global rainfall and circulation patterns<sup>1</sup>. ENSO has a profound impact on the inter-annual as well as the intra-seasonal variabilities of the Indian summer monsoon (ISM)<sup>2–6</sup>. The Summer ENSO index is negatively correlated with the ISM seasonal rainfall, and the strength of the ENSO-ISM relation in models is a preeminent indicator of the seasonal predictability of the ISM rainfall<sup>7</sup>. The well-known inverse relationship between the ENSO and the ISM seasonal rainfall has weakened in the late 20th century<sup>8</sup> and it was largely restored in the early part of the 21st century<sup>9,10</sup>. Several studies have been devoted to finding the reason for the weakening of this relationship at the end of the last century. These studies came up with various conclusions alluding to the effects of all different phenomena including: the Atlantic Multi-decadal Oscillation<sup>11</sup>; the co-occurrence of IOD events with El Niño<sup>12</sup> (like Goswami and An<sup>13</sup> in a hypothetical climate change context); the shift in the ENSO center of action<sup>14</sup>; changes in the convection patterns over the equatorial Indian Ocean<sup>15,16</sup>; circulation changes in the equatorial Indian Ocean and south-east of Japan<sup>17</sup>; the strengthening of the sub-tropical jet stream over the North Atlantic<sup>18</sup>; and global warming<sup>8</sup>. Sterl et al.<sup>19</sup>, has shown that the sampling variability can explain most of the apparent changes in the running-window “apparent” ENSO teleconnection and, likewise, Yun & Timmermann<sup>20</sup> and Bódai et al.<sup>21</sup> have pointed out that the stochastically perturbed ENSO signal can generate fluctuations similar to the observed changes in the ENSO-ISM teleconnection, contradicting, thus, at least Kumar et al.<sup>8</sup>. On the other hand, the *recovery* of the apparent ENSO-ISM rainfall relation during the early 21st century received less attention. It was attributed e.g. by Yang & Huang<sup>9</sup> to the inter-decadal variation of ENSO’s evolution and related changes in the tropical Atlantic Ocean.

As for future projections of the ENSO-ISM rainfall relationship, especially of the sign of the trend, Lee & Bódai<sup>22</sup> prompted the possibility of a large uncertainty. Still, several studies led to a pertinent conclusion that the inverse relationship between ENSO and the ISM rainfall will prevail in future global warming scenarios<sup>21–26</sup>. Ashrit et al.<sup>23</sup> examined a transient climate simulation from a single model and have indicated that the impact of El Niño events on the ISM rainfall will decrease in future, while the impact of La Niña events will remain largely unchanged. Li & Ting<sup>26</sup> examined CMIP5 model simulations and claimed that the ENSO-ISM rainfall relation could slightly weaken in the 21st century. Roy et al.<sup>27</sup> analyzed a subset of the CMIP5 dataset and reported a strengthening of the ENSO-ISM teleconnection during future canonical and mixed canonical modoki ENSO events, and a weakening of the teleconnection during modoki events. Pandey et al.<sup>28</sup> reported that the long-term relationship between ENSO-ISM rainfall will change from negative to positive under the global warming scenario. They performed the correlation analysis without removing the long-term trend from the ISM rainfall and Pacific SST. If we retain the long-term trend in the CMIP6 multi-model mean analysis, the teleconnection strength will weaken at the end of the 21st century; otherwise, it will be stationary<sup>22</sup>. Two recent studies<sup>25,29</sup> utilizing the finite size but so-called “large initial condition ensemble” simulation of the Max Planck Institute Grand Ensemble (MPI-GE) concluded that the ENSO-ISM teleconnection strengthens in the 21st century, with a slow-down at the end of the century. The conclusion was reached by performing statistical tests of non-stationarity, detecting a signal masked strongly by large statistical error fluctuations. This also means that the precise magnitude of the change is even more hopeless to correctly predict.

These initial condition ensemble-based studies suggest thus that the quantification of the forced response of the ENSO-ISM teleconnection is sensitive to a divergence from the correct

<sup>1</sup>Center for Climate Physics, Institute for Basic Science (IBS), Busan 46241, Republic of Korea. <sup>2</sup>Pusan National University, Busan 46241, Republic of Korea. <sup>3</sup>Department of Applied Statistics, Hungarian University of Agriculture and Life Sciences, Budapest, Hungary. ✉email: aneesh.ply@gmail.com; bodait@yahoo.com

methodology<sup>29</sup> and to the datasets utilized<sup>22</sup>. I.e., the offerings of single model studies, like Bódai et al.<sup>29</sup> and Goswami and An<sup>13</sup> are very limited. From the observational data or single realization of a model, on the other hand, even the sign of the forced response of the teleconnection is impossible to determine because of the inability of the temporal methods to distinguish the changes caused by internal variability and external forcing factors<sup>21,29</sup>. In principle, the forced response can be properly disentangled from the internal variability by using an initial condition large ensemble simulation<sup>29,30</sup>. However, in fact, the ensemble methods are also burdened by biases concerning certain statistical estimators<sup>25</sup> due to the sampling error caused by the finite size of the ensemble members, as well as due to the inherent model errors. Concerning the latter, as also advocated by Lee and Bódai<sup>22</sup>, the use of *multi-model* large initial condition ensemble simulations would be rather informative to evaluate the *robustness* of the forced response of any observable of the climate system across the climate models by means of evaluating it properly first in each individual model and, subsequently, by comparison. Recent studies have used multi-model large initial condition ensemble simulation data to address different scientific questions such as: the uncertainties in the projection of global monsoon precipitation<sup>31</sup>; the projection of ENSO variance<sup>32</sup>; the role of the interdecadal Pacific oscillation in the near-term projection uncertainties of the ISM<sup>33</sup>; the internal variability of different climate modes<sup>34</sup>; and the calculation of the time of emergence of biogeochemically important upper-ocean variables<sup>35</sup>.

In the present study, as the first such multi-model study, we use nine different climate models with 30 or more ensemble members to estimate the historical and future forced changes of the ENSO-ISM relation. We find that the internal variability of the climate system is primarily responsible for the observed weakening of the ENSO-ISM rainfall relationship in the late 20th century. The forced response of the ENSO-ISM relationship in the first half of the 21st century, at a coarse temporal view, is either strengthening or stationary, and the robustness diminishes in the second half. Furthermore, the study addresses the relative role of ENSO variability, coupling strength, and noise strength in the projected changes of the ENSO-ISM rainfall teleconnection.

## RESULTS

### Forced evolution of the ENSO-ISM teleconnection and its driving factors

Basic skills of the selected nine models such as in simulating the mean state and variability of the ISM and ENSO and the ENSO-ISM teleconnection, are evaluated by comparing the corresponding observations during the 1950–2020 period with the ensemble spread (Supplementary Fig. 1). On the one hand, all the models have good to reasonable skill in capturing the ENSO variability, i.e., the Niño3.4 SST anomaly during the historical period fall within the ensemble spread. On the other hand, even though the majority of the models could reasonably simulate the ISM rainfall variability and ENSO-ISM correlation coefficient, the performance of the CanESM5 and CSIRO-MK-3.6 was relatively weak. However, we caution as to disregarding a model wrt. the forced change of the ENSO-ISM teleconnection, because the skill in reproducing the mean state does not have universally clear implications on the skill in reproducing the forced change of the same quantity. In this regard, we walk back on the view of Bódai et al.<sup>29</sup> dropping the analysis of the CESM1 model. Furthermore, we note that, as per, e.g. (Yun & Timmermann<sup>20</sup>; Bódai et al.<sup>21</sup>), the available observational data is insufficient in assessing model skill wrt. the forced change of the ENSO-ISM teleconnection. Therefore, in our analysis of the inter-model robustness of the latter, we keep all the models that we have data for.

Bódai et al.<sup>25</sup> have identified three drivers of the ENSO-ISM teleconnection strength, namely: ENSO variability ( $\sigma_\phi$ ), the ENSO-ISM coupling strength measured by the regression coefficient ( $a$ ), and the noise strength ( $\sigma_\varepsilon$ ). These are related to the ENSO-ISM correlation coefficient through the textbook formula

$$r = \frac{1}{\sqrt{1 + ((\sigma_\varepsilon/a)/\sigma_\phi)^2}} \quad (1)$$

based on a simple linear regression model. Each year, the ensemble-wise correlation coefficient  $r$  is estimated, and the time-evolution  $r(t)$  of the correlation coefficient describes the forced change, bar the masking effect of rather large statistical errors. Similarly, the time series of each driver, estimated with respect to the variability across the ensemble members, prompts potentially its relative “contribution” or role to the forced change of the correlation coefficient  $r$ . Bódai et al.<sup>25</sup> also introduced a simple framework for the quantitative estimate of the relative role of  $\sigma_\phi$  and  $a/\sigma_\varepsilon$  in the time interval  $t_1$  and  $t_2$ . The parameters  $\beta = \sigma_\phi(t_2)/\sigma_\phi(t_1)$  and  $\alpha = (\sigma_\varepsilon(t_2)/a(t_2))/(\sigma_\varepsilon(t_1)/a(t_1))$  are estimated over different time intervals and the product of  $\alpha$  and  $\beta$  determines the relative impact of drivers  $\sigma_\phi$  and  $a/\sigma_\varepsilon$  on the forced change of  $r$ . We adopt here approach used by Bódai et al.<sup>25</sup> to calculate the forced change in the teleconnection strength and its statistical attribution to the drivers (see their section 2.3). The time-evolution of  $-r(N, A|t)$  between Niño3.4 SST ( $N$ ) and the All-India summer monsoon (AISMR,  $A$ ) rainfall (averaged over the Indian landmass excluding the observational data sparse regions: see Fig. 1 of Parthasarathy et al.<sup>36</sup>) for the nine models is depicted in Fig. 1a and the other rows are similar but show the (b) ENSO variability  $\sigma_\phi$ , (c) ratio of coupling strength and noise strength  $a/\sigma_\varepsilon$ , (d) coupling strength  $a$  and (e) noise strength  $\sigma_\varepsilon$ , respectively. Supplementary Fig. 2 also shows the projected changes in the correlation coefficients and their drivers but uses Niño3 SST instead of Niño3.4 SST. In general, Fig. 1 and Supplementary Fig. 2 show similar patterns in the projected correlation coefficient, even though the magnitude of the projected change varies in some models.

The smoothed time series of the correlation coefficient (Fig. 1a) shows characteristic ups and downs in all the models, and the temporal evolutions  $r(t)$  do not have a common pattern between the models. The statistical significance of the non-stationarity of the correlation coefficient in all possible time intervals is tested by the Mann-Kendall test (following Bódai et al.<sup>25,29</sup>), whose test statistics, corresponding to each model, are shown in Fig. 2. Also, the corresponding statistical significance for Supplementary Fig. 2a is depicted in Supplementary Fig. 3. On the long-term, between e.g., 1950–2100, the CanESM5, CanESM2, CSIRO MK-3.6 and ACCESS ESM1-5 models show statistically significant strengthening of the teleconnection, especially at the end of the 21st century (Fig. 1). While, in contrast, the GFDL ESM2M and MIROC6 models depict a significant weakening of the teleconnection. Thirdly, the MPI-ESM, GFDL SPEAR, and CESM2 models barely show any significant change in the teleconnection in the 1950–2100 period. However, the MPI-ESM and GFDL SPEAR models depict a strengthening of the projected teleconnection if we use the Niño3 SST instead of Niño3.4 SST (Supplementary Fig. 3). In what follows, we look at the drivers of any change in  $r(t)$ .

We start with  $\sigma_\phi$ . It is claimed that there is a lack of inter-model consensus in the projected ENSO SST variability in the CMIP5 models<sup>37</sup> whereas the majority of the CMIP6 models show an enhancement in the ENSO SST variability<sup>38</sup>. The time series of the ensemble-wise standard deviation of Niño3.4 SST ( $\sigma_\phi$ ) from the nine climate models are depicted in Fig. 1b, and for Niño3 SST, it is depicted in Supplementary Fig. 2b. The temporal patterns of the forced changes in the Niño3.4 SST variability show a good resemblance with those in the Niño3 SST. Every model shows a non-monotonic change in the projected standard deviation of

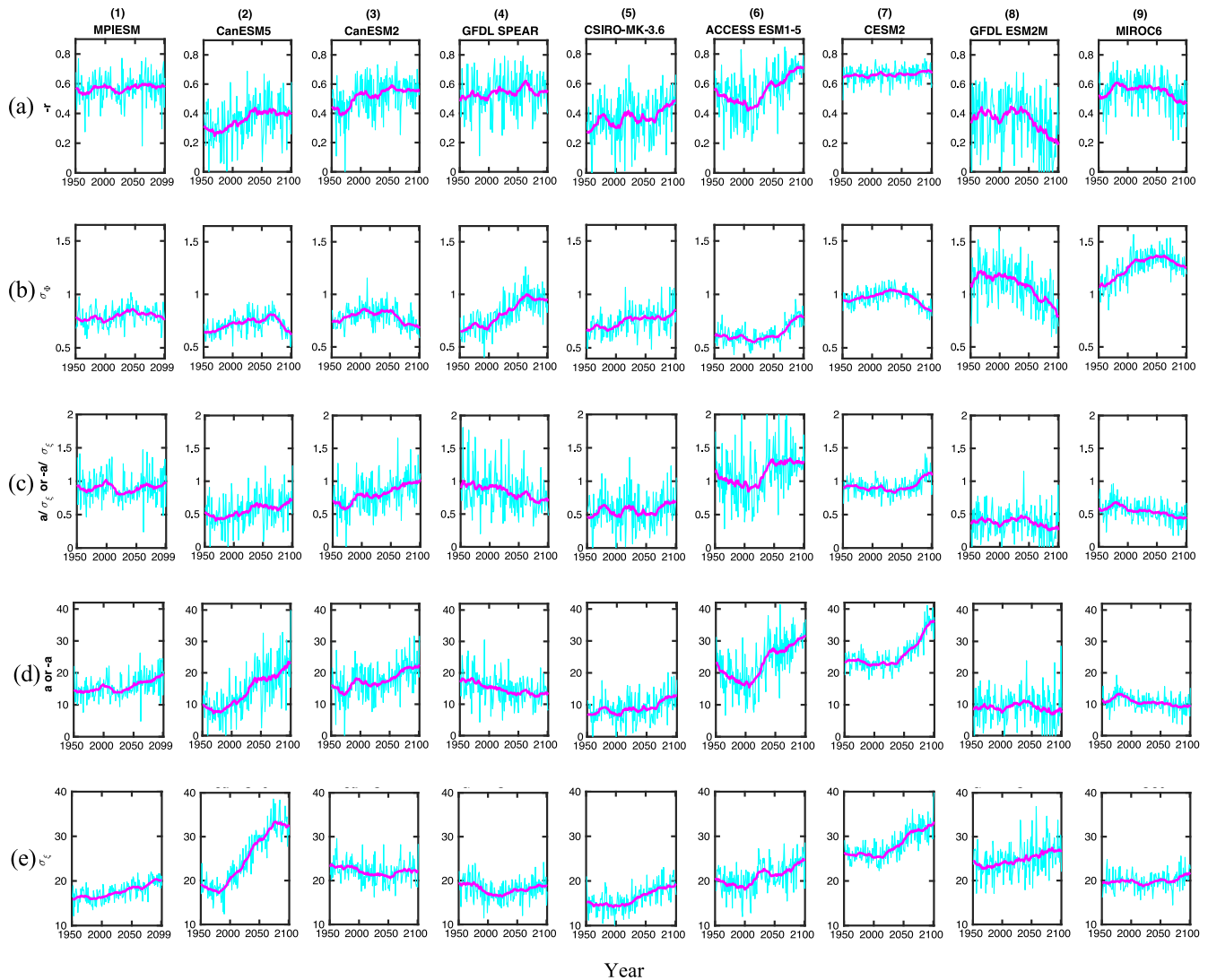


**Fig. 1** Forced changes in the correlation coefficient and its drivers. **a** displays the time-evolution of the ensemble-wise correlation coefficients ( $-r$ ), between the Niño3.4 SST and AISMR during the 1950–2100 period from 9 models (columns 1–9). The Pearson correlation coefficient is calculated in each year between the Niño3.4 SST and AISMR, which corresponds to first removing the corresponding years' ensemble mean from individual ensemble members. The other rows are analogous to **a**, but for the **b** ENSO variability, **c** ENSO-ISM coupling strength/noise strength, **d** ENSO-ISM coupling, and **e** noise strength. Magenta curves show 21-year moving means, and cyan curves show the "raw" yearly values. All the calculations for the MPI-ESM model are done using the data up to 2099.

Niño 3/3.4 SST; however, their rate of change is model-dependent. The MPI-ESM, CanESM5, GFDL SPEAR, CESM2, and MIROC6 models depict a gradual increase in the ensemble-wise standard deviation until around the mid/late 21st century and a decline after that, i.e., nonmonotonicity. In the CanESM2 model, the standard deviation does not change much in the first half of the 21st century, while it shows a sharp decline in the later half. In contrast, the GFDL ESM2M model shows a decline in the standard deviation throughout the 21st century, whereas CSIRO-MK-3.6 and ACCESS ESM1-5 shows an increase at the end of the 21st century. The non-monotonic time evolution of the projected ENSO amplitude is also reported in Kim et al.<sup>39</sup>. It is attributed there to the difference in the east-west surface warming rate over the Indo-Pacific region.

Moving on, considering the next driver, the time-evolution of the projected changes in the regression coefficient  $a$  (coupling strength), shows a strengthening in the 21st century in most of the models, except for the GFDL SPEAR, GFDL ESM2M and MIROC6 (Fig. 1d). The coupling strength is nearly stagnant in the GFDL ESM2M, whereas GFDL SPEAR and MIROC6 show a slightly decreasing trend in the 21st century.

Finally, the forced evolution of the standard deviation and mean of the June to September (JJAS) ISM rainfall averaged over the Indian landmass (AISMR) are shown in Supplementary Fig. 4. The simulated mean monsoon rainfall shows a large inter-model difference, with the lowest amount of rainfall in the CSIRO-MK-3.6 and the highest in the MIROC6 model. However, every model except for GFDL ESM2M shows an increase in the mean monsoon rainfall in the 21st century. Thus, most of the models used in the present study agree with previous reports that the mean seasonal rainfall over the Indian region will increase under unabated global warming in the 21st century<sup>40–42</sup>. On the other hand, the projected ISM rainfall variability, whose change should be related to that of the mean in different models, is found here to be either increasing or non-decreasing. The MPI-ESM, CanESM5, CSIRO-MK-3.6, CESM2, and GFDL ESM2M models show an increasing trend in the ISM rainfall variability in the 21st century, whereas the CanESM2, GFDL SPEAR, and MIROC6 models do not show any notable change in the future.

Even though ENSO is the dominant external factor that modulates the interannual variability of the ISM<sup>2,43</sup>, the ISM

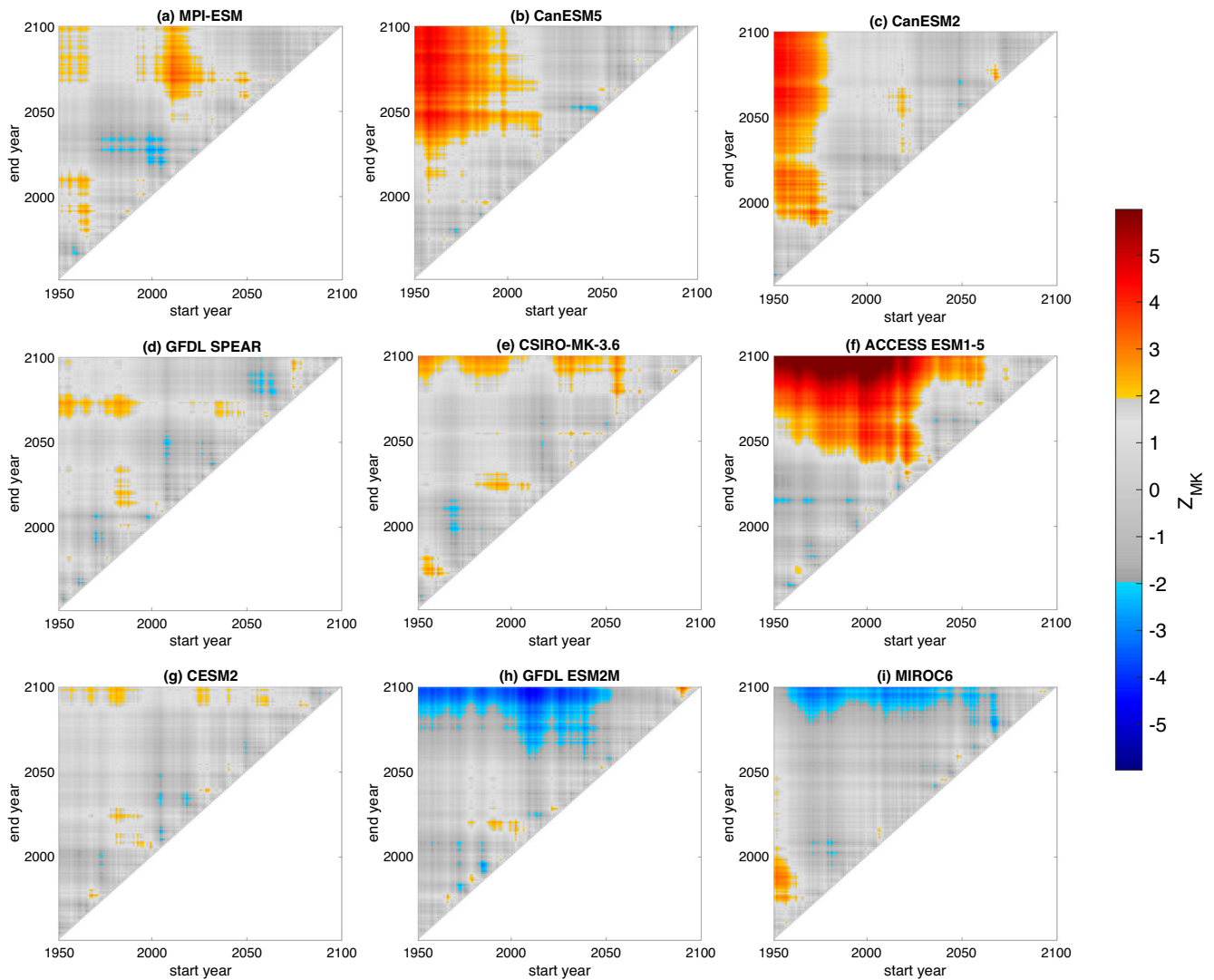


**Fig. 2** Statistical significance of the forced change of the ENSO-ISM relation. **a–i** depicts the Mann–Kendall test statistics for the stationarity of correlation coefficient ( $-r$ ) between the Niño3.4 SST and AISMR, from 9 models. Red and blue shades show statistically significant trends ( $p$  value  $< 0.05$ ), i.e., the detection of non-stationarity.

variability in most of the models does not follow a non-monotonic pattern like the ENSO variability observed in Fig. 1b. In the beginning and middle of the 21st century, most of the climate models project an increasing trend in the ISM variability like ENSO variability changes. At the end of the 21st century, however, the covariance is lost in the climate models. This points out the presence of some other mechanism, which masks the influence of the declining ENSO variability on the ISM variability at the end of 21st century. Meehl & Arblaster<sup>44</sup> has shown that the warmer Pacific Ocean is the primary cause of the enhancement of the interannual variability of the ISM in a global warming scenario, while the Indian Ocean warming plays a secondary role. Thus, the tug-of-war between the opposite impacts of decreasing ENSO variability and the increasing Indo-Pacific SST, and the changes in the other internal and external factors may have resulted in the increasing or non-decreasing ISM variability at the end of the 21st century. The time series of the forced response of the noise strength  $\sigma_{\xi}(t)$  is comparable to the ISM rainfall variability (Fig. 1e, Supplementary Fig. 2e, Supplementary Fig. 4). The forced changes in the noise strength show an increasing trend in most of the models, except for the CanESM2 model. The maximum increasing trend in the noise strength and the ISM rainfall variability is noted

in the CanESM5. The relative role of each driving factor in the forced change of the ENSO-ISM teleconnection is addressed in the next sessions.

### The role of external forcing and internal variabilities in the observed weakening of the ENSO-ISM relation at the end of the 20th century

During the second half of the 20th century, the correlation coefficient does not show a significant change in most of the models, while CanESM2 and MIROC6 showed a slight statistically significant strengthening due to the increasing ENSO variability and the coupling strength in this period. This is in contrast with the *apparent* weakening of the ENSO-ISM teleconnection in the observational data during the end of the 20th century<sup>8</sup>, with a magnitude drop of approximately 0.4 in the 21-year moving window correlation coefficient (after about 1980). However, the change in the ensemble-wise correlation coefficient should be less than 0.1 in the selected nine models. This suggests that the weakening of the ENSO-ISM (JJA Niño3.4 SST–JJAS AISMR) teleconnection after  $\sim 1980$  is in large part due to internal climate variability, and the anthropogenic forcing has an undetectable

role in it<sup>21</sup>. Although it is still an open question how much the true forced change was in reality, whether the models could systematically overlook some of it.

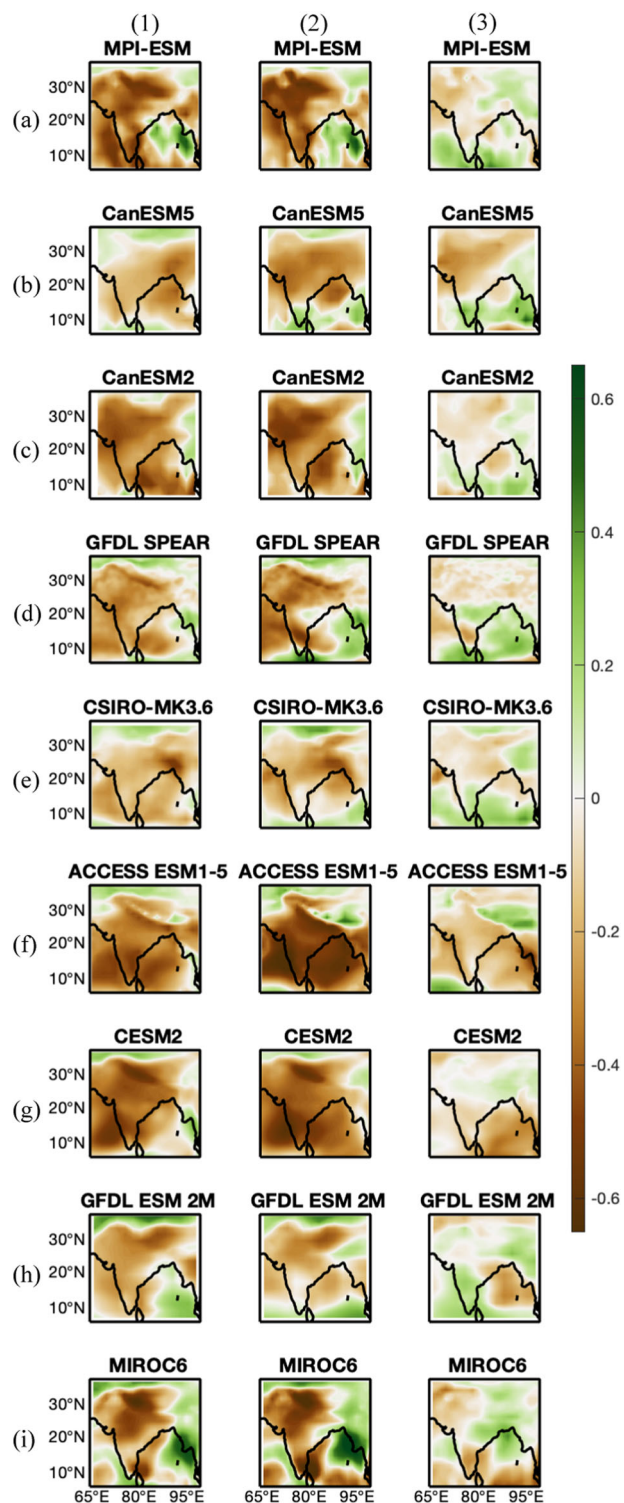


**Fig. 3** Historical and future changes in the spatial pattern of the correlation coefficient  $r$ . The first column displays  $r$  between the grid-wise ISM precipitation and the first principal component corresponding to the EOF1 of the tropical Pacific SST during 1950–2000, from nine models (rows a–i). The second column is the same as the first, but for the period 2050–2100. The third shows the difference in  $r$ : “2050–2100 minus 1950–2000”.

### The relative role of driving factors in the forced change of ENSO-ISM teleconnection in the 21st century

During the first half of the 21st century, the ENSO-ISM teleconnection, with a coarse view of time (disregarding the short-term significant changes), is either strengthening or non-decreasing in all models. The CanESM5, CanESM2, and ACCESS ESM1-5 models show an increase in the correlation coefficient, whereas, in the other models, the correlation coefficient does not show any significant change during this period. The increase in ENSO variability and the coupling coefficient favored (Eq. (1)) the strengthening of the correlation coefficient in the CanESM5 and ACCESS ESM1-5 models (in CanESM2, only the coupling coefficient increases). The relative “contribution”, or influence, of ENSO variability ( $\sigma_\phi$ ) versus the ratio of the coupling and noise strengths ( $a/\sigma_\varepsilon$ ) in increasing the correlation coefficient ( $-r$ ) is shown in Supplementary Fig. 5 (See Section 2.3 of Bódai et al.<sup>25</sup> for the method). The figure indicates that  $a/\sigma_\varepsilon$  has relatively more influence than  $\sigma_\phi$  in strengthening teleconnection (since  $a\beta < 1$  in most of the periods) during the first half of 21st century. On the other hand, even though both the ENSO variability and the coupling coefficient have increased in the MPI-ESM, CSIRO-MK-3.6 and CESM2 models, the relative increase of noise strength reduced the ratio  $a/\sigma_\varepsilon$  and resulted in a stagnant correlation coefficient. In the GFDL ESM2M model, furthermore, the decline of ENSO variability starts in the early 21st century already and it is balanced by the simultaneous increase of the coupling coefficient. In the MIROC6 and GFDL SPEAR model, the stationarity is due to the balance between the increasing ENSO variance and decreasing coupling coefficient. Thus, there is no inter-model consensus on the source of the observed stationarity in the first half of the 21st century.

In the second half of the 21st century, the teleconnection is stationary in the MPI-ESM, CanESM5, CanESM2, GFDL SPEAR, and CESM2 models; whereas ACCESS ESM1-5 and CSIRO-MK-3.6 shows a significant strengthening of the teleconnection, and the GFDL ESM-2M and MIROC6 models show a significant weakening of the teleconnection during the same period. The stationarity in the MPI-ESM, CanESM5, CanESM2, and CESM2 models is primarily due to the balance between the decreasing ENSO variability and the simultaneously increasing coupling coefficient. The strengthening of the teleconnection in the ACCESS ESM1-5 and CSIRO MK-3.6 models is mainly due to the still continuing increase of ENSO variability at the end of 21st century. Meanwhile, the decrease in the coupling coefficient observed in the GFDL ESM-2M and MIROC6 models at the end of the 21st century led to the weakening of the teleconnection. Thus, there is hardly any robustness in the forced response of the teleconnection at end of the 21st century simulations.

### Spatial patterns of the correlation coefficient

The spatial patterns of the correlation coefficient between the principal component of the first EOF pattern of the Pacific SST over the domain 30°S–30°N and 110°E–65°W and rainfall over India and nearby regions during the second half of the 20th and second half of the 21st century are shown in the first two columns of Fig. 3. Even though there are inter-model differences in the spatial patterns of the correlation coefficient, all models display a negative correlation over the Indian landmass. A positive correlation coefficient occurs over the central and eastern part of the Bay of Bengal in the MPI-ESM, GFDL ESM-2M, and MIROC6 models, however, the correlation coefficient there is negative in other models. The forced change of the correlation coefficient between the second half of the 21st century and the second half of the 20th century is displayed in the third column of Fig. 3. The MPI-ESM, CanESM5, CanESM2, CSIRO MK-3.6 and ACCESS ESM1 models show a strengthening of the teleconnection in most part of India except for eastern and southern (except ACCESS ESM1)

peninsular India. Thus, the models showing a strengthening (weakening) of the teleconnection in the 21st century, as seen in Fig. 1a, are those that display an overwhelmingly positive (negative) change in the AISMR domain. Even though the CESM2 model did not show any forced change in the area averaged ISM rainfall, it displays a weak strengthening of the teleconnection in peninsular India and weakening in the central-eastern part of India—largely balanced in magnitude and spatial extension. In the GFDL ESM 2 M model, a weakening of the teleconnection is noted in most parts of India. In MIROC6, central-eastern peninsular India and the west coast show a weakening, and the central-eastern part of peninsular India, and the north-western part of India display a strengthening of the teleconnection. The leading EOF pattern of ISM rainfall and its future changes are shown in Supplementary Fig. 6. Since the first EOF pattern of ISM rainfall is significantly correlated with the ENSO<sup>45</sup>, the projected changes in the leading EOF patterns of rainfall have a close correspondence with the future changes in the spatial pattern of  $r$  in Fig. 3, except for the CanESM2 model. In a nutshell, we found a robust strengthening of the projected teleconnection over north-west India and a robust weakening over the north-eastern part of India, while the forced change in teleconnection is highly non-robust over central India due to a variation of the (i) demarcation line of positive and negative changes and the (ii) magnitude of those changes. This indicates that while the physical explanation of the decreasing teleconnection strength found by Goswami and An<sup>13</sup> might be sound, there is little value in learning about it.

#### Physical mechanism responsible for the forced change of the coupling coefficient

The non-robustness noted in the forced response of the ENSO-ISM teleconnection in the 21st century has a profound connection with the forced changes in the coupling strength  $a$ . The coupling

strength shows a slight decreasing trend in the GFDL ESM2M and MIROC6 models, whereas a significant increasing trend is simulated by the other seven models. The forced changes in the spatial patterns of the tropical Pacific SST could, in principle, have an impact on the projected coupling strength. The summer EOF1 pattern of the tropical Pacific SST during the 1950–2000 and 2050–2100 periods are depicted in Supplementary Fig. 7 first and second column (a–i) respectively. The difference between the EOF1 patterns between the two periods is shown in Supplementary Fig. 7a–i. Every model could reasonably well simulate the typical EOF1 pattern of the tropical Pacific SST. The forced response in the CMIP6 models (CanESM5, GFDL SPEAR, ACCESS ESM1-5, CESM2, and MIROC6) bear some resemblance with respect to the spatial pattern, with enhanced variability over the central-eastern equatorial Pacific Ocean and reduced variability over the western part. However, the SST patterns of CMIP5 models do not show any inter-model consensus. The forced change in the MPI-ESM is not prominent; the GFDL ESM 2 M closely resembles the CMIP6 models, while the CanESM2 and CSIRO-MK-3.6 models show a reduction in their respective variability over the eastern equatorial Pacific Ocean. Hence, it is clear that the forced changes in the spatial pattern of the tropical Pacific SST does not play any significant role in the projected strengthening or weakening of the coupling strength.

The ACCESS ESM1-5 and CESM2 models simulate strong positive trends in *coupling coefficient* and MIROC6 simulates the largest negative trend in the second half of the 21st century. Therefore, we selected these three models, the ACCESS ESM1-5, CESM2 and MIROC6, to find the physical mechanism responsible for the said opposing responses. The spatial maps of the “climatological” Niño3.4 SST regressed precipitation (i.e., the maps of the regression coefficient for the local precipitation *anomalies* versus Niño3.4 SST anomalies, lumped with respect to both

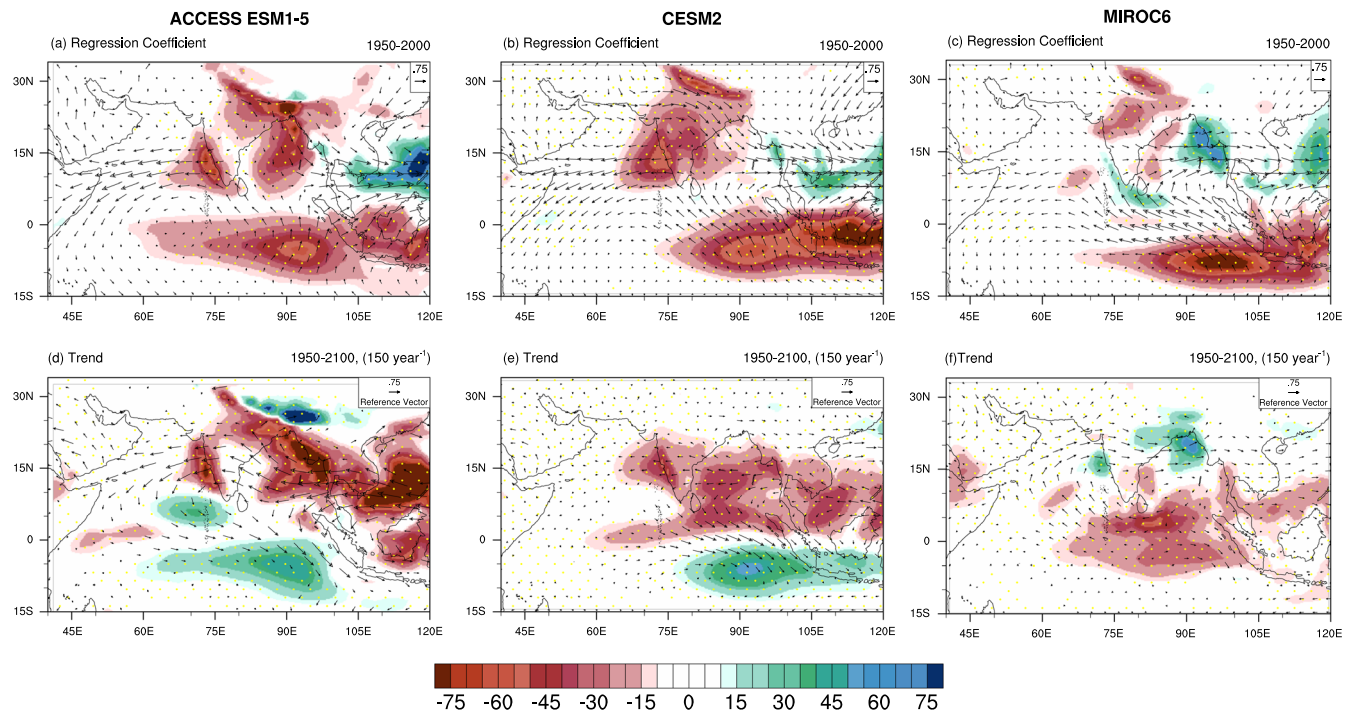
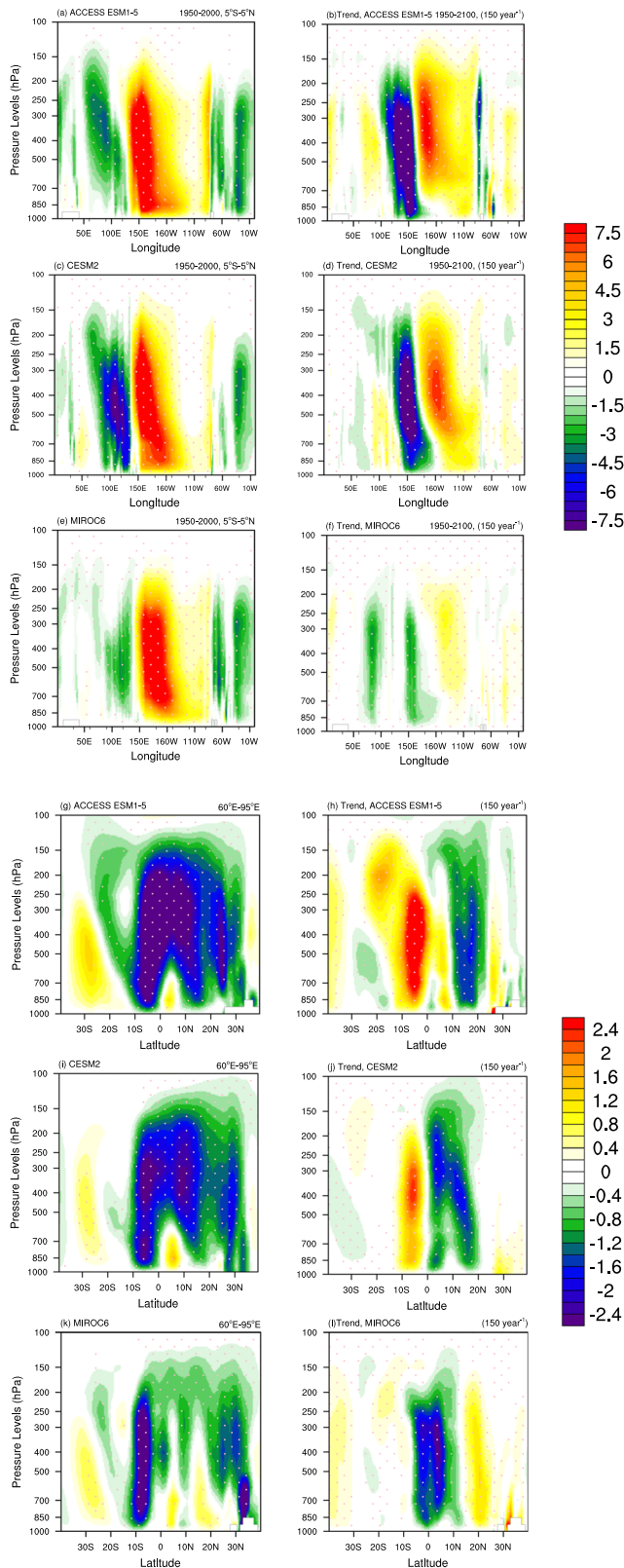


**Fig. 4** Climatology and forced changes in the Niño3.4 SST regressed precipitation and LLJ anomalies. The color shading in a–c shows the regression strength of Niño3.4 SST (JJA) vs precipitation (JJAS mean) anomalies, and the arrows represent the regression on the wind at 850 hPa, from the ACCESS ESM1-5, CESM2, and MIROC6 models, respectively. These analyses were carried out during the historical period 1950–2000. The yellow dots represent the regions where the sign of the regression coefficient is the same for >95% of the years during the period of 1950–2000. d–f are similar to a–d, but for the trend (150 year<sup>-1</sup>) in the regression coefficient over the 1950–2100 period. Only the statistically significant (above 95%) trends in the Niño3.4 SST regressed wind at 850 hPa are shown by arrows. The regions having statistically significant trend in Niño3.4 SST regressed precipitation are marked with yellow dots.



ensemble members and time; color shading) and low-level winds at 850 hPa (arrows), calculated from the ACCESS ESM1-5, CESM2 and MIROC6 models during the 1950–2000 period, are depicted in Fig. 4a–c. All the models simulate a negative regression coefficient (with precipitation) over the Indian region and the eastern part of

**Fig. 5** Climatology and forced changes in the Niño3.4 SST regressed Walker and regional Hadley circulations. **a** Longitude-altitude cross-section of the Niño3.4 SST (JJA mean) regressed Omega (JJAS mean, multiplied by  $-300$ ), averaged over the latitude band  $5^{\circ}\text{S}$ – $5^{\circ}\text{N}$ , calculated from the ACCESS ESM1-5 large ensemble data during the 1950–2000 period. **b** is the same as **a**, but for the trend ( $150\text{ year}^{-1}$ ) of the regression coefficient over the 1950–2100 period. **c**, **d** are the same as **a**, **b**, respectively, but for the CESM2 model. **e**, **f** are from the MIROC6 model. **g**–**l** is similar to **a**–**f**, but for the latitude-altitude cross-sections of Omega, which is averaged over the longitudinal band of  $60^{\circ}\text{E}$ – $95^{\circ}\text{E}$ . The dotted regions in the trend figures show statistically significant linear trend values (above 95% confidence), and the dotted regions in the regression coefficient figures show the consistency of the sign of the regression coefficient (95% of the time) during the 1950–2000 period.

the equatorial Indian Ocean. Even though the regression patterns show some resemblance, the magnitude of the regression coefficients over the Indian region is weak in the MIROC6 model in comparison with ACCESS ESM1-5 and CESM2. The regression pattern of wind at 850 hPa in the three models depicts a weakening of the monsoon low-level jet (LLJ) over the Arabian Sea and a strengthening of wind intrusion to the central part of India. The weakening of the LLJ and enhancement of dry wind intrusion to central India can reduce the ISM rainfall<sup>46</sup>. Thus, the strong negative coupling coefficient simulated by the ACCESS ESM1-5 and CESM2 models is linked to the changes in the wind pattern. The *trend* in the regression coefficients of Niño3.4 SST anomalies versus precipitation and wind anomalies at 850 hPa are depicted in Fig. 4d–f. In the ACCESS ESM1-5 and CESM2 models, the coupling between ENSO and rainfall strengthens over the Indian landmass and the Bay of Bengal, whereas it weakens over the eastern equatorial Indian Ocean. I.e., the future El Niño (La Niña) events can bring about more anomalous reduction (enhancement) of rainfall over peninsular India and the Bay of Bengal region. The enhanced drying during positive ENSO years is partly due to the weakening of the LLJ over peninsular India and nearby oceanic parts and vice versa. Meanwhile in MIROC6, future El Niño events can cause more anomalous rainfall over the west coast of peninsular India, the central-eastern part of India and the Bay of Bengal due to the strengthening of the LLJ.

The ENSO-induced anomalous changes in the regional Hadley and Walker circulation during the 1950–2000 “climatological” period and its future changes are shown in Fig. 5. Panels a, c, f display the Niño3.4 SST regressed vertical velocity Omega (multiplied by  $-300$ ) averaged over the latitude band of  $5^{\circ}\text{S}$ – $5^{\circ}\text{N}$  from the three selected models, representing the influence of ENSO on the Walker cells. All the models simulate an anomalous eastward shift of the Walker cell over the Pacific Ocean. In comparison with the MIROC6 model, the ACCESS ESM1-5 and CESM2 models simulate a strong ENSO-induced anomalous descending motion over the eastern part of the Indian Ocean and the western part of the Pacific Ocean. Forced trends of the Niño3.4 SST regressed Walker circulation over the 1950–2100 period are shown in Fig. 5b, d, f. All the models project *more/stronger* ENSO-induced anomalous eastward shifts in the Walker cell over the Pacific Ocean *under global warming*, however, maximum shift is observed in both ACCESS ESM1-5 and CESM2. Otherwise, the models show contrasting features over the Indian Ocean. The MIROC6 model simulates a strong descending motion over the Indian Ocean whereas the CESM2 and ACCESS ESM1-5 models show an opposite trend over the Indian Ocean. This can significantly modulate the projected ENSO influence on the regional Hadley cell over the ISM region and the SST pattern over the Indian Ocean.

During the ISM season, strong convection is observed over the Indian landmass and nearby oceanic parts, and a strong

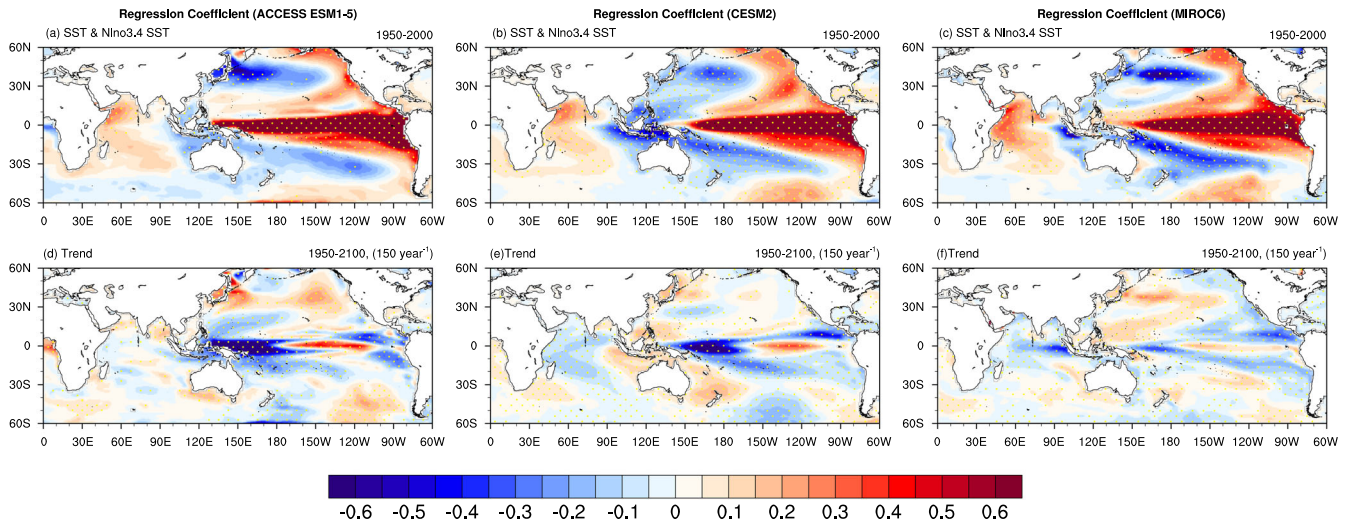


**Fig. 6** Climatology and forced changes in the Niño3.4 SST regressed Indo-Pacific SST. **a–c** show the Niño3.4 SST (JJA mean) regressed SST (JJAS mean) over the Indo-Pacific region during the 1950–2000 period, from the ACCESS ESM1-5, CESM2 and MIROC6 models, respectively. The corresponding trends ( $150 \text{ year}^{-1}$ ) in the regression coefficients over the 1950–2100 period are shown in **d–f**. The yellow dots in **d, f** represent the regions with statistically significant ( $p < 0.05$ ) trend, and in **a–c** they show the regions where the sign of the regression coefficient is consistent (same for more than 95% of time).

descending motion over the southern Indian Ocean. These ascending and descending branches are parts of the regional Hadley cell, whose interannual variability is significantly modulated by ENSO. ENSO's influence on the regional Hadley cell and its future projections are shown in Fig. 5g–l, by calculating the regression coefficient of Niño3.4 SST versus Omega (multiplied by  $-300$ ) and its trend. The regional Hadley circulation is represented as a latitude-altitude cross-section by taking the  $60^{\circ}\text{E}$ – $95^{\circ}\text{E}$  longitudinal average. All the models simulated negative (positive) regression coefficients over latitudes of peninsular India (the southern Indian Ocean), which reveals a large-scale suppression (enhancement) of the convection during El Niño (La Niña) events. The suppression of convection over the Indian latitude is more prominent in the ACCESS ESM1-5 and CESM2 models, which is in support of the strong ENSO-ISM coupling observed in Fig. 4a, c. The trend analysis of the Niño3.4 SST regressed regional Hadley cell (Fig. 5h, j, l) shows contrasting, entirely different patterns between MIROC6 and the other two models. In ACCESS ESM1-5 and CESM2, equatorial convection has strengthened, and more suppression of convection is observed over the Indian latitudes under the future global warming scenario. At the same time, in MIROC6, the convection over the equatorial Indian ocean and the Indian region have weakened and strengthened, respectively. These forced changes in the ENSO-induced convection patterns favor the strengthening versus weakening of the ENSO-ISM rainfall coupling in the ACCESS ESM1-5/CESM2 versus MIROC6 models, respectively.

The Niño3.4 SST regressed Indo-Pacific SST patterns during the “climatological” period 1950–2000 and the forced trend in the ensemble-wise regression coefficient over 1950–2100 period are evaluated in the three models and pictured in Fig. 6. In general, the regression map generated from the three model simulations resemble an El Niño-like pattern in the tropical Pacific Ocean and a positive IOD-like pattern in the Indian Ocean. However, the regression pattern simulated by the models over the oceanic parts surrounding the Maritime continent region are distinct, a strong negative regression coefficient is noted in CESM2, whereas such a prominent pattern is comparatively weaker in the other two models. Furthermore, the positive regression coefficient noted in the western Indian Ocean and the Arabian sea are stronger in MIROC6 in comparison with the other models. The trend analysis shows that all three models project a reduction of the regression

coefficient over the western part of the equatorial Pacific Ocean and an increase over the central-eastern part of the equatorial Pacific Ocean in the future. This pattern is more evident in the ACCESS ESM1-5 and CESM2 model, and it is linked to the eastward shift in the Walker circulation as seen in Fig. 5. At the same time, the projected patterns over the off-equatorial Pacific Ocean and the Indian Ocean do not show good resemblance between the models. The projected changes in the SST regression pattern in the ACCESS ESM1-5 model shows a strengthening of the positive correlation coefficient over the Bay of Bengal and the northern part of the Arabian Sea, and the CESM2 model shows a weakening of the IOD-like SST pattern. Even though the ACCESS ESM1-5 and MIROC6 model projected an increasing trend in the coupling coefficient as well as a similar pattern in the projected Walker cell, their impact on the Indian Ocean SST is different. Goswami, 2023<sup>47</sup> has reported that the eastern equatorial Indian Ocean warming can increase the convection over the west coast of Sumatra, its atmospheric response can weaken the monsoon LLJ and thereby reduce the ISM rainfall. Similarly in our analyses seen above, the future projection of the ENSO-ISM coupling simulated by the CESM2 model shows an increase in the equatorial convection, weakening of the LLJ, and decrease of the ISM rainfall in the positive phase of ENSO. This might be partially linked to the reduction in the anomalous cooling of the eastern equatorial Indian Ocean and the changes in the regional Hadley circulation. However, the MIROC6 model simulations show a strengthening and widening the area of the negative correlation observed in the eastern part of the equatorial Indian Ocean. I.e., a strong cooling of SST can occur over the central and eastern part of the equatorial Indian Ocean during the positive phase of ENSO events in the future. Consequently, it suppresses the equatorial convection and thereby reduces the rainfall over the equatorial Indian Ocean, as observed in Fig. 4f. The atmospheric response to this convective anomaly can strengthen the LLJ and enhance the ISM rainfall.

## DISCUSSION

The present study investigates the forced changes of the ENSO-ISM teleconnection in the historical and future high emission scenarios, using a multi-model ensemble of large initial condition ensemble simulations of climate models. We applied a proper statistical technique to disentangle the forced changes in the



ENSO-ISM teleconnection from the noisy internal variability in all the models—as far as possible, pending the ensemble size. We analyzed the relative role of the different factors responsible for the teleconnection change and unraveled the physical mechanism responsible for the difference in the forced change of the coupling strength between models. The latter plays a crucial role in the lack of inter-model robustness at the end of the 21st century.

As an attainable ambition, we try to determine at least the sign of a forced change of the teleconnection per model. In two models investigated previously<sup>13,29</sup>, the signs were opposing. Observational studies suggest a weakening of the ENSO-ISM inverse relationship, particularly at the end of the 20th century. However, the time evolution of the ensemble-wise correlation coefficient between the Niño3/3.4 SST and ISM rainfall evaluated in each climate model failed to detect a significant weakening of the teleconnection during the same period. Thus, the observed weakening of the teleconnection seems likely due to the internal variability of the climate system, i.e., it is probably not at all externally forced.

In the first half of the 21st century, the long-term trend of the teleconnection strength is either increasing or stationary in the models. Most of the models show a strengthening of the three driving factors, namely: ENSO variability, the coupling strength, and noise strength, during this period. The increase of the former two driving factors strengthens the teleconnection, and that of the latter one weakens the teleconnection strength as indicated by Eq. (1). The time evolution of at least two driving factors in all the models is in favor of the increase in the teleconnection strength, even though their rate of change varies across the models. Consequently, the tug-of-war between the three driving factors resulted in a medium degree of robustness, that is, the teleconnection is strengthening or stationary. There is a lack of robustness in the forced response of the teleconnection strength in the latter half of the 21st century. A robust decrease in ENSO variability (except for CSIRO-MK-3.6 and ACCESS ESM1-5) and an increase in the coupling coefficient (except for GFDL SPEAR, GFDL ESM2M, and MIROC6) are observed in most of the climate models. The strength of the forced response of the teleconnection is mainly determined by the competing rates of change of ENSO variability and the rate of change of the coupling strength, which are not modeled robustly.

We also examined the physical mechanisms behind the contrasting trends in the projected coupling strength between the ACCESS ESM1-5, CESM2, and MIROC6 models in the 21st century. All the selected models simulated an eastward shift in the ENSO-related Walker cell anomalies over the Pacific Ocean in the future. However, models in which the coupling coefficient strengthens (ACCESS ESM1-5 and CESM2) or weakens (MIROC6) in future simulated contrasting effects on the regional Hadley circulation. This might have resulted in the opposite trends in the forced response of the coupling strength.

The common biases in climate models over the tropical Pacific Ocean are the “cold tongue bias” and “double ITCZ bias”<sup>48,49</sup>. The double ITCZ bias is present in all the generations of Coupled Model Intercomparison Project (CMIP), even though the bias has slightly reduced in the latest generation as of writing, the CMIP6<sup>49</sup>. The cold tongue bias also exists in all the CMIP versions, but the inter-model spread has reduced from CMIP5 to CMIP6<sup>49</sup>. These biases can impact the future projection of the ENSO variabilities and its teleconnections. The majority of CMIP6 models show a future enhancement in the ENSO variability (Niño3/Niño3.4 SST variance) and extreme ENSO events<sup>38</sup>. However, the forced time-evolution of the Niño3 SST variability is non-monotonic in the majority of models, and large inter-model differences are present.

The skill of the climate models in representing the ISM is improving in every new CMIP version<sup>50,51</sup>. The projected increase in the mean ISM rainfall and inter-annual variability is more robust in CMIP6 in comparison with CMIP5<sup>40</sup>. However, still, there is still

no inter-model agreement in the magnitude of the projected changes in the ISM precipitation and the variabilities of the ISM<sup>50</sup> including those influenced by ENSO. The improvements in the physical parameterization schemes and perhaps using a high-resolution for simulations can significantly reduce the biases in the simulated ISM<sup>52</sup> and ENSO variabilities<sup>53</sup>. The reduction of model errors should improve the ENSO-ISM teleconnection in climate models, too, which would give rise to more robust projections of this very important relationship.

## METHODS

### Large ensemble and observational data

We analyzed nine simulated so-called “large initial condition ensemble” datasets having at least 30 ensemble members per model, in which four models are of CMIP5 class and the others are of CMIP6 (Supplementary Table 1). However, we used all the available ensemble members from the selected models, to get a more statistically accurate evaluation of the forced response. The study spans a period between year 1950 of the historical simulation to year 2100 of the future projection scenarios (RCP8.5/SSP585/SSP370). The CMIP5 class models used are: MPI-ESM-LR<sup>54</sup>, CanESM2<sup>55</sup>, CSIRO-MK-3.6<sup>56</sup>, and GFDL ESM2M<sup>57</sup>. The CMIP6 class models are: CESM2<sup>58</sup>, MIROC6<sup>59</sup>, CanESM5<sup>60</sup>, GFDL SPEAR<sup>61</sup> and ACCESS ESM1-5<sup>62</sup>. The SST dataset used is the Met Office Hadley Center’s sea ice and sea surface temperature (HadiSST)<sup>63</sup> and the precipitation dataset used is the Climatic Research Unit gridded Time Series-4 (CRU TS v4)<sup>64</sup>.

### Snapshot EOF analysis

The snapshot EOF (SEOF) analysis is applied to the tropical Pacific SST as done in Bódai et al.<sup>25</sup>. In the SEOF method, EOFs are calculated with respect to variability across the ensemble members rather than time<sup>25,65</sup>. Although, a lumping of data in a desirably short time window is beneficial in reducing finite-size errors as well as biases. In the SEOF method, first we remove each year’s ensemble mean from that year’s individual ensemble members, which will retain only the signal of internal variability. Then the EOF pattern of each year is calculated across the ensemble members. Each year’s EOF patterns are averaged for the required period to get the final EOF pattern.

### ENSO-ISM teleconnection and the Mann–Kendall test statistics

The ENSO-ISM teleconnection is represented as the ensemble-wise correlation coefficient evaluated each year between the June to September average of the All-India summer monsoon (AISMR<sup>36</sup>) and the June to August average of the Niño3/Niño3.4 SST (having naturally removed the ensemble mean from each ensemble member). The time evolution of the correlation coefficient evaluated in this way corresponds to the forced change of the teleconnection in that climate model<sup>25</sup>. The forced change in the spatial pattern of the correlation coefficient is evaluated between the precipitation over the Indian region and the SEOF1 of the tropical Pacific SST. The Mann-Kendall test is performed in order to determine the significance of non-stationarity of the correlation coefficient, the same way as calculated in Bódai et al.<sup>25,29</sup>. The normally distributed test statistics are denoted as  $Z_{MK}$ , which retains the sign of the trend. To get more insight into the time dependence of non-stationarity, the test is done in all the possible time intervals.

### DATA AVAILABILITY

The HadiSST<sup>63</sup> data are available at <https://www.metoffice.gov.uk/hadobs/hadisst/data/download.html>. The CRU TS V4<sup>64</sup> precipitation data was downloaded from <https://crudata.uea.ac.uk/cru/data/hrg/>. The MPI-ESM-LR<sup>54</sup>, CanESM2<sup>55</sup>, CSIRO-MK-3.6<sup>56</sup>, and GFDL ESM2M<sup>57</sup> large ensemble data are publicly available at the National

Center for Climate Research (NCAR) climate data gateway [https://www.earthsystemgrid.org/dataset/ucar.cgd.cesm4.CLIVAR\\_LE.html](https://www.earthsystemgrid.org/dataset/ucar.cgd.cesm4.CLIVAR_LE.html). The ACCESS ESM1-5<sup>62</sup>, MIROC6<sup>59</sup>, and CanESM5<sup>60</sup> large ensemble data are publicly accessible via the CMIP server <https://esgf-node.lln.gov/search/cmip6/>. The GFDL SPEAR<sup>61</sup> large ensemble data can be downloaded from the Geophysical Fluid Dynamics Laboratory (GFDL) website [https://www.gfdl.noaa.gov/spear\\_large\\_ensembles/](https://www.gfdl.noaa.gov/spear_large_ensembles/). The CESM2<sup>58</sup> large ensemble data is publicly available at <https://www.earthsystemgrid.org/dataset/ucar.cgd.cesm2le.output.html>. Also, the processed datasets used in the present study are available from the corresponding authors upon reasonable request.

## CODE AVAILABILITY

The source codes for the data analysis and visualization are available from the corresponding authors upon reasonable request.

Received: 6 April 2023; Accepted: 5 December 2023;

Published online: 02 January 2024

## REFERENCES

- Ropelewski, C. F. & Halpert, M. S. Global and regional scale precipitation patterns associated with the El Niño/Southern oscillation. *Mon. Weather Rev.* **115**, 1606–1626 (1987).
- Dwivedi, S., Goswami, B. N. & Kucharski, F. Unraveling the missing link of ENSO control over the Indian monsoon rainfall. *Geophys. Res. Lett.* **42**, 8201–8207 (2015).
- Goswami, B. N. & Xavier, P. K. ENSO control on the south Asian monsoon through the length of the rainy season. *Geophys. Res. Lett.* **32**, L18717 (2005).
- Mooley, D. A. & Parthasarathy, B. Indian summer monsoon and El Niño. *Pure Appl. Geophys.* **121**, 339–352 (1983).
- Rajeevan, M. & Pai, D. S. On the El Niño-Indian monsoon predictive relationships. *Geophys. Res. Lett.* **34**, L04704 (2007).
- Sperber, K. R., Slingo, J. M. & Annamalai, H. Predictability and the relationship between subseasonal and interannual variability during the Asian summer monsoon. *Q. J. R. Meteorol. Soc.* **126**, 2545–2574 (2000).
- Jain, S., Scaife, A. A. & Mitra, A. K. Skill of Indian summer monsoon rainfall prediction in multiple seasonal prediction systems. *Clim. Dyn.* **52**, 5291–5301 (2019).
- Kumar, K. K., Rajagopalan, B. & Cane, M. A. On the weakening relationship between the Indian monsoon and ENSO. *Science* **284**, 2156–2159 (1999).
- Yang, X. & Huang, P. Restored relationship between ENSO and Indian summer monsoon rainfall around 1999/2000. *Innovation* **2**, 100102 (2021).
- Yu, S.-Y., Fan, L., Zhang, Y., Zheng, X.-T. & Li, Z. Reexamining the Indian summer monsoon rainfall–ENSO relationship from its recovery in the 21st century: role of the Indian ocean SST anomaly associated with types of ENSO evolution. *Geophys. Res. Lett.* **48**, e2021GL092873 (2021).
- Chen, W., Dong, B. & Lu, R. Impact of the Atlantic Ocean on the multidecadal fluctuation of El Niño–Southern Oscillation–South Asian monsoon relationship in a coupled general circulation model. *J. Geophys. Res.: Atmos.* **115**, D17109 (2010).
- Ashok, K., Guan, Z. & Yamagata, T. Impact of the Indian Ocean dipole on the relationship between the Indian monsoon rainfall and ENSO. *Geophys. Res. Lett.* **28**, 4499–4502 (2001).
- Goswami, B. B. & An, S.-I. An assessment of the ENSO-monsoon teleconnection in a warming climate. *npj Clim. Atmos. Sci.* **6**, 82 (2023).
- Kumar, K. K., Rajagopalan, B., Hoerling, M., Bates, G. & Cane, M. Unraveling the mystery of Indian monsoon failure during El Niño. *Science* **314**, 115–119 (2006).
- Aneesh, S. & Sijikumar, S. Changes in the La Niña teleconnection to the Indian summer monsoon during recent period. *J. Atmos. Sol. Terr. Phys.* **167**, 74–79 (2018).
- Sreejith, O. P., Panickal, S., Pai, S. & Rajeevan, M. An Indian Ocean precursor for Indian summer monsoon rainfall variability. *Geophys. Res. Lett.* **42**, 9345–9354 (2015).
- Feba, F., Ashok, K. & Ravichandran, M. Role of changed Indo-Pacific atmospheric circulation in the recent disconnect between the Indian summer monsoon and ENSO. *Clim. Dyn.* **52**, 1461–1470 (2019).
- Chang, C.-P., Harr, P. & Ju, J. Possible roles of Atlantic circulations on the weakening Indian monsoon rainfall–ENSO relationship. *J. Clim.* **14**, 2376–2380 (2001).
- Steril, A., van Oldenborgh, G. J., Hazeleger, W. & Burgers, G. On the robustness of ENSO teleconnections. *Clim. Dyn.* **29**, 469–485 (2007).
- Yun, K.-S. & Timmermann, A. Decadal monsoon-ENSO relationships reexamined. *Geophys. Res. Lett.* **45**, 2014–2021 (2018).
- Bódai, T., Lee, J.-Y. & Aneesh, S. Sources of nonergodicity for teleconnections as cross-correlations. *Geophys. Res. Lett.* **49**, e2021GL096587 (2022).
- Lee, J.-Y. & Bódai, T. In: Indian Summer Monsoon Variability (eds. J. Chowdary, A. Parekh, & C. Gnanaseelan) 393–412 (Elsevier, 2021).
- Ashrit, R. G., Kumar, K. R. & Kumar, K. K. ENSO-monsoon relationships in a greenhouse warming scenario. *Geophys. Res. Lett.* **28**, 1727–1730 (2001).
- Azad, S. & Rajeevan, M. Possible shift in the ENSO-Indian monsoon rainfall relationship under future global warming. *Sci. Rep.* **6**, 20145 (2016).
- Bódai, T., Drótos, G., Ha, K.-J., Lee, J.-Y. & Chung, E.-S. Nonlinear forced change and nonergodicity: the Case of ENSO-Indian Monsoon and Global Precipitation Teleconnections. *Front. Earth Sci.* **8**, 599785 (2021).
- Li, X. & Ting, M. Recent and future changes in the Asian monsoon-ENSO relationship: natural or forced? *Geophys. Res. Lett.* **42**, 3502–3512 (2015).
- Roy, I., Tedeschi, R. G. & Collins, M. ENSO teleconnections to the Indian summer monsoon under changing climate. *Int. J. Climatol.* **39**, 3031–3042 (2019).
- Pandey, P., Dwivedi, S., Goswami, B. N. & Kucharski, F. A new perspective on ENSO-Indian summer monsoon rainfall relationship in a warming environment. *Clim. Dyn.* **55**, 3307–3326 (2020).
- Bódai, T., Drótos, G., Herein, M., Lunkeit, F. & Lucarini, V. The forced response of the El Niño–Southern Oscillation–Indian monsoon teleconnection in ensembles of earth system models. *J. Clim.* **33**, 2163–2182 (2020).
- Drótos, G., Bódai, T. & Tél, T. Probabilistic concepts in a changing climate: a snapshot attractor picture. *J. Clim.* **28**, 3275–3288 (2015).
- Zhou, T., Lu, J., Zhang, W. & Chen, Z. The sources of uncertainty in the projection of global land monsoon precipitation. *Geophys. Res. Lett.* **47**, e2020GL088415 (2020).
- Maher, N., Matei, D., Milinski, S. & Marotzke, J. ENSO change in climate projections: forced response or internal variability? *Geophys. Res. Lett.* **45**, 11,390–11,398 (2018).
- Huang, X. et al. South Asian summer monsoon projections constrained by the interdecadal Pacific oscillation. *Sci. Adv.* **6**, eaay6546 (2020).
- Fasullo, J. T., Phillips, A. S. & Deser, C. Evaluation of leading modes of climate variability in the CMIP archives. *J. Clim.* **33**, 5527–5545 (2020).
- Schlunegger, S. et al. Time of emergence and large ensemble intercomparison for ocean biogeochemical trends. *Glob. Biogeochem. Cycles* **34**, e2019GB006453 (2020).
- Parthasarathy, B., Munot, A. A. & Kothawale, D. R. All-India monthly and seasonal rainfall series: 1871–1993. *Theor. Appl. Climatol.* **49**, 217–224 (1994).
- Taschetto, A. S. et al. Cold tongue and warm pool ENSO events in CMIP5: mean state and future projections. *J. Clim.* **27**, 2861–2885 (2014).
- Cai, W. et al. Changing El Niño–Southern Oscillation in a warming climate. *Nat. Rev. Earth Environ.* **2**, 628–644 (2021).
- Kim, S. T. et al. Response of El Niño sea surface temperature variability to greenhouse warming. *Nat. Clim. Change* **4**, 786–790 (2014).
- Katzenberger, A., Schewe, J., Pongratz, J. & Levermann, A. Robust increase of Indian monsoon rainfall and its variability under future warming in CMIP6 models. *Earth Syst. Dyn.* **12**, 367–386 (2021).
- Menon, A., Levermann, A., Schewe, J., Lehmann, J. & Frieler, K. Consistent increase in Indian monsoon rainfall and its variability across CMIP-5 models. *Earth Syst. Dyn.* **4**, 287–300 (2013).
- Turner, A. G. & Annamalai, H. Climate change and the South Asian summer monsoon. *Nat. Clim. Change* **2**, 587–595 (2012).
- Webster, P. J. et al. Monsoons: processes, predictability, and the prospects for prediction. *J. Geophys. Res.: Oceans* **103**, 14451–14510 (1998).
- Meehl, G. A. & Arblaster, J. M. Mechanisms for projected future changes in south Asian monsoon precipitation. *Clim. Dyn.* **21**, 659–675 (2003).
- Mishra, V., Smoliak, B. V., Lettenmaier, D. P. & Wallace, J. M. A prominent pattern of year-to-year variability in Indian summer monsoon rainfall. *Proc. Natl Acad. Sci.* **109**, 7213–7217 (2012).
- Aneesh, S. & Sijikumar, S. Changes in the south Asian monsoon low level jet during recent decades and its role in the monsoon water cycle. *J. Atmos. Sol. Terr. Phys.* **138–139**, 47–53 (2016).
- Goswami, B. B. Role of the eastern equatorial Indian Ocean warming in the Indian summer monsoon rainfall trend. *Clim. Dyn.* **60**, 427–442 (2023).
- Mechoso, C. R. et al. The seasonal cycle over the tropical Pacific in coupled ocean–atmosphere general circulation models. *Mon. Weather Rev.* **123**, 2825–2838 (1995).
- Tian, B. & Dong, X. The double-ITCZ Bias in CMIP3, CMIP5, and CMIP6 Models based on annual mean precipitation. *Geophys. Res. Lett.* **47**, e2020GL087232 (2020).
- Gusain, A., Ghosh, S. & Karmakar, S. Added value of CMIP6 over CMIP5 models in simulating Indian summer monsoon rainfall. *Atmos. Res.* **232**, 104680 (2020).
- Sperber, K. R. et al. The Asian summer monsoon: an intercomparison of CMIP5 vs. CMIP3 simulations of the late 20th century. *Clim. Dyn.* **41**, 2711–2744 (2013).
- Ramu, D. A. et al. Indian summer monsoon rainfall simulation and prediction skill in the CFSv2 coupled model: impact of atmospheric horizontal resolution. *J. Geophys. Res.: Atmos.* **121**, 2205–2221 (2016).

53. Liu, B. et al. Will increasing climate model resolution be beneficial for ENSO simulation? *Geophys. Res. Lett.* **49**, e2021GL096932 (2022).
54. Maher, N. et al. The Max Planck institute grand ensemble: enabling the exploration of climate system variability. *J. Adv. Model. Earth Syst.* **11**, 2050–2069 (2019).
55. Kirchmeier-Young, M. C., Zwiers, F. W. & Gillett, N. P. Attribution of extreme events in arctic sea ice extent. *J. Clim.* **30**, 553–571 (2017).
56. Jeffrey, S. et al. Australia's CMIP5 submission using the CSIRO-Mk3.6 model. *Aust. Meteorol. Oceanogr. J.* **63**, 1–13 (2013).
57. Rodgers, K. B., Lin, J. & Frölicher, T. L. Emergence of multiple ocean ecosystem drivers in a large ensemble suite with an Earth system model. *Biogeosciences* **12**, 3301–3320 (2015).
58. Rodgers, K. B. et al. Ubiquity of human-induced changes in climate variability. *Earth Syst. Dynam.* **2021**, 1–22 (2021).
59. Tatebe, H. et al. Description and basic evaluation of simulated mean state, internal variability, and climate sensitivity in MIROC6. *Geosci. Model Dev.* **12**, 2727–2765 (2019).
60. Swart, N. C. et al. The Canadian earth system model version 5 (CanESM5.0.3). *Geosci. Model Dev.* **12**, 4823–4873 (2019).
61. Delworth, T. L. et al. SPEAR: the next generation GFDL modeling system for seasonal to multidecadal prediction and projection. *J. Adv. Model. Earth Syst.* **12**, e2019MS001895 (2020).
62. Ziehn, T. et al. The Australian earth system model: ACCESS-ESM1.5. *J. South. Hemisph. Earth Syst. Sci.* **70**, 193–214 (2020).
63. Rayner, N. A. et al. Global analyses of sea surface temperature, sea ice, and night marine air temperature since the late nineteenth century. *J. Geophys. Res.: Atmos.* **108**, 4407 (2003).
64. Harris, I., Osborn, T. J., Jones, P. & Lister, D. Version 4 of the CRU TS monthly high-resolution gridded multivariate climate dataset. *Sci. Data* **7**, 109 (2020).
65. Haszpra, T. & Topál, D. & Herein, M. On the time evolution of the arctic oscillation and related wintertime phenomena under different forcing scenarios in an ensemble approach. *J. Clim.* **33**, 3107–3124 (2020).

## ACKNOWLEDGEMENTS

S.A. was supported by the Institute for Basic Science (IBS), Republic of Korea, under IBS-R028-D1, and T. Bódai under IBS-R028-Y1. The analysis was conducted on the IBS/ICCP supercomputer “Aleph,” 1.43 peta flops high-performance Cray XC50-LC Skylake computing system with 18,720 processor cores, 9.59 PB storage, and 43 PB tape archive space. We also acknowledge the support of KREONET.

## AUTHOR CONTRIBUTIONS

S.A.: investigation, analysis, visualization, prepared the original draft with the help of T.B., editing and reviewing. T.B.: conceptualization, writing, reviewing, editing, and supervision.

## COMPETING INTERESTS

The authors declare no competing interests.

## ADDITIONAL INFORMATION

**Supplementary information** The online version contains supplementary material available at <https://doi.org/10.1038/s41612-023-00541-w>.

**Correspondence** and requests for materials should be addressed to Sundaresan Aneesh or Tamás. Bódai.

**Reprints and permission information** is available at <http://www.nature.com/reprints>

**Publisher's note** Springer Nature remains neutral with regard to jurisdictional claims in published maps and institutional affiliations.



**Open Access** This article is licensed under a Creative Commons Attribution 4.0 International License, which permits use, sharing, adaptation, distribution and reproduction in any medium or format, as long as you give appropriate credit to the original author(s) and the source, provide a link to the Creative Commons license, and indicate if changes were made. The images or other third party material in this article are included in the article's Creative Commons license, unless indicated otherwise in a credit line to the material. If material is not included in the article's Creative Commons license and your intended use is not permitted by statutory regulation or exceeds the permitted use, you will need to obtain permission directly from the copyright holder. To view a copy of this license, visit <http://creativecommons.org/licenses/by/4.0/>.

© The Author(s) 2024